Magnetizable Concrete Flux Concentrators for Wireless Inductive Power Transfer Applications

C. Carretero, *Senior Member, IEEE,* I. Lope, *Member, IEEE,* and J. Acero *Member, IEEE,*

***Abstract*—Wireless inductive power transfer (IPT) systems incorporate magnetic flux concentrators in order to improve some features, as coupling and efficiency, and also to reduce electromagnetic emissions. Usually, flux concentrators consist of ferrite cores, which are arranged according to the size and shape of inductive power pads and also according to the application. Ferrite is the most common magnetic material due to its optimal balance between performance and cost. Despite the availability of ferrite cores with a wide set of shapes and sizes, in some applications the optimal matching between inductive power paths and flux concentrators becomes problematic. In this work, magnetic cement concrete is evaluated as a size-adaptable material for the arrangement of flux concentrators of IPT systems. Both cement powder and concrete are magnetically characterized at different temperature, field level and frequencies, and measurements show that the achieved levels of permeability, Curie's temperature and losses make this material attractive for potential flux concentrator uses. A potential IPT application is evaluated by means of a finite element study and the results are applied to a prototype design. Feasibility of use of the magnetic cement is tested by means of different power pads according to different flux concentrator arrangements.**

***Index Terms*—Inductive power transmission, electromagnetic induction, ferrites, mutual coupling, magnetic properties.**

I. Introduction

INDUCTIVE power transfer (IPT) applications have attracted a massive attention of both academy and industry in recent years since its wireless nature confers superior advantages with respect to traditional power transfer technologies [1]–[3]. This technology finds application in many spheres of daily life as electric vehicles (EVs), medical devices, consumer electronics or harsh environments [4]–[8]. Currently, wireless battery chargers, including static [9] or dynamic [10], [11] charging systems, are one of most relevant applications of IPT technology with power rating ranging from some watts up to several kW, and a potential market of more than 1$ billion [2]. Apart from the mentioned application, IPT systems are currently spreading its application range and inspiring new uses. In this spirit, applications as battery chargers for autonomous underwater vehicles [12], power transference systems with oscillating magnets [13], multi-transmitter systems with optimized receivers [14] or wireless systems incorporating intermediate resonators [15] are of current interest.

C. Carretero is with the Department of Applied Physics, University of Zaragoza, Spain.

I. Lope is with BSH Home Appliances, Zaragoza, Spain and with the Department of Applied Physics, University of Zaragoza, Spain.

J. Acero is with the Department of Electronic Engineering and Communications, University of Zaragoza, Spain.

Therefore, an intensive research activity is currently devoted to different aspects of the magnetic coupler, due to its implications in the performance of the whole system. In this way, in some work,s a field-shape configuration to minimize the leakage flux was proposed [16], [17]. Moreover, arrangements for reconfigurable IPT systems [18], IPT structures with arbitrary number of coils [16], [17], [19], and dipole-coil arrangements [20]–[22] were recently proposed. Often, design methodologies can also be found in the recent literature [23]–[25].

In general terms, IPT systems exploit a varying magnetic flux for transferring energy between two coils, or equivalently. To some extent, IPT systems operate as a transformer where alternating voltage is induced between two loosely coupled coils. Fig. 1 shows the basic elements of an IPT system, which comprises two planar coils and their corresponding flux concentrators (usually called TX and RX power pads) and shielding. Despite the obvious similarities between IPT systems and transformers, they also present substantial differences. Apart from coil shape, the reluctance of IPT systems is higher than in conventional transformers because the magnetic flux path include a large air gap. High reluctance causes low magnetic coupling, high leakage inductances, high electromagnetic emissions and low equivalent impedance. The influence of these aspects on the electronic converter design is of capital importance. Moreover, depending on the coil arrangement, the proximity losses of windings can be penalized in the case of low magnetic coupling [26], with the subsequent reduction of efficiency.

IPT systems are mainly arranged by means of two elements, namely, multistranded ($litz$) wires for windings and ferrite cores for flux concentrators [27]–[34]. With respect to the windings, few alternatives to litz wires have been proposed. PCB coil implementations [35], [36], hollow rectangular conductors [37], printed windings by means of inkjet technology [38], and copper tubes [39] are some examples.

Regarding flux concentrators, alternatives to ferrite cores have been rarely proposed. Flux concentrators are placed in IPT systems with the purpose of improving the coupling between transmitter and receiver. Considering that a magnetic material adjacent to a winding can be approximated with a current image distribution [40], [41], it follows that flux concentrator arrangements should adapt to the size and shape of windings in order to achieve the optimal result. Ferrite cores are commonly used due to its good balance between cost, performance and availability. Most applications only use a core shape (i.e. E-, U-, I-cores) [28], [30], [42], [43], whereas combinations of cores are less frequent [5], [27], [44]. In

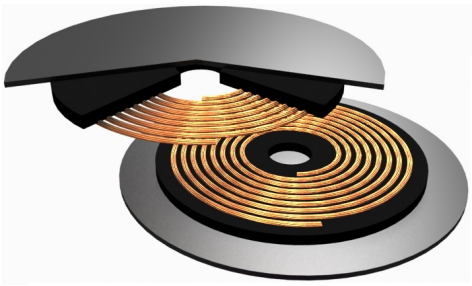

Fig. 1: Representation of an IPT system comprising the transmitter and receiver power pads.

some applications, the matching between windings and flux concentrators may become cumbersome [45], [46]. Moreover, the brittle behaviour of ferrites could be an additional issue in applications where power pads are under pressure, impacts or load variations.

Recently, magnetizable concretes for IPT applications (Magment^{TM}) have been developed [47] and tested [48] with the purpose of enhancing the magnetic coupling of on-line battery chargers for EVs. Regarding the Magment, according to manufacturer's information it is a composite material consisting of a cement matrix loaded with magnetizable particles. As a result, according to manufacturer's data initial relative permeability up to 40 can be reached in the cured material, which could be suitable for IPT uses. Moreover, magnetizable concrete allows to implement stiff magnetics, mechanically stable and corrosion resistant devices with long service life. Magnetizable concretes could be an interesting alternative to ferrite cores for implementing configurable flux concentrators, if magnetic properties are adequate. For this reason, properties of magnetizable concrete should be properly characterized, specially magnetic permeability, maximum flux density, Curie temperature, and losses at different field level, temperature and frequency conditions. Some of these properties are provided by the manufacturer, but others not provided, as the permeability with respect to temperature and field level, can be of interest for designers. Flux concentrators based on magnetic powder, i.e. ferrite green powder or ferrite filings, could constitute an additional possibility. However, this option requires a container for the powder and could lead to air pollution during manufacturing due to fine dust particles.

In this work firstly we present the characterization results of the aforementioned properties. Moreover, other aspects as properties of the different phases of the material (i.e. sifted cement, cement and concrete), and minimum permeability or thickness for a specific application are also investigated. These results complements the information provided by magnetizable concrete manufacturers [47] and therefore they can be used to propose innovative solutions for challenging aspects of practical applications. The performance of a practical IPT system featuring magnetizable concrete in the TX power pad is tested by means of an experimental setup which is previously analyzed by means of finite element simulations.

This paper is mainly focused on the electrical parameters of power pads constructed with the selected magnetic concrete following the instructions provided by the manufacturer. Therefore, mechanical or constructive aspects, i.e. curing and compressive strength, are beyond the scope of this paper. Similarly, aspects referring to power electronics or compensation networks are also not considered in this work. Apart from these considerations, other innovations addressed in the paper are:

- Analysis of the temperature operating range of the different phases of the magnetizable concrete, or equivalently, analysis of the Curie's temperature of the magnetic elements of the concrete.
- Analysis of the permeability of the magnetizable concrete phases (dust, bits, concrete).
- Breakdown of winding losses considering the coupling effects between coils.
- Comparison of the electrical parameters of power pads with different arrangements: air, ferrite sheet and concrete disk.
- Study of the concrete thickness required for achieving an equivalent performance with respect to ferrite sheet.

The paper is organized as follows. In Section II the characterization method is described and results are presented. The characterization is obtained by means of toroids of four samples with different processing. The electromagnetic analysis of the IPT system is presented in Section III. This analysis is accomplished by means of the COMSOL^{TM} Finite Element Analysis (FEA) tool. The encountered permeability requirements for achieving an acceptable efficiency are presented and highlighted in a detailed discussion. In Section IV the details on the experimental setup and results under both low signals and high signal conditions are presented. Results of tests with special attention on mutual inductance and frequency-dependent losses are also presented. Section V discusses some practical aspects, as the design for the concrete sheet that match with the ferrite performance. Finally, in Section VI, the main conclusions obtained in this work are summarized.

II. Characterization of magnetizable concrete

A simple visual inspection of MC40 cement, Fig. 3(a), shows that it consists of ferrite bits and dust. These phases can be separated by screening, as it is shown in Fig. 3(b). Size of ferrite bits ranges from 2 mm to 8 mm whereas the dust consists of magnetic and non-magnetic particles, where the former can be separated by means of a magnet. Magnetic particles could be ferrite filings of the same specimen as bits. The weight proportion of the different phases of the commercial material were measured giving the approximate composition of the MC40 shown in Table I. Regarding this table, the characterization of the following cases is considered of interest:

- Sifted MC40 cement.
- Concrete based on sifted MC40.
- MC40 cement.
- MC40 concrete.

Characterization of the two cements could be of interest for implement flux concentrators by means of a free-shape mould which is filled with cement. Concrete is made by adding water to the cement in the proportion indicated by the manufacturer.

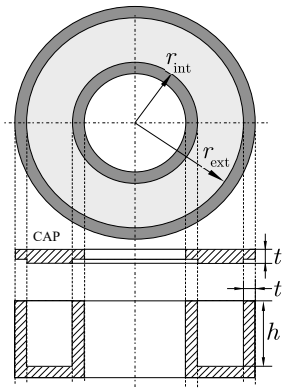

Fig. 2: Schematic representation of the mould for making toroidal samples.

Wounded toroids are chosen for characterization purposes because magnetic flux is continuous in this geometry and boundary conditions of Maxwell's equations allow to predict the magnetic field strenght inside the toroid with respect to the winding current. Therefore, equivalent magnetic permeabilty of material can be deduced from electrical measurements obtained with a high precision LCR meter. Internal dimensions of toroids, i.e., effective dimensions of the material under study, are listed as follows: external radius $r_{\text{ext}} = 20.75$ mm, internal radius $r_{\text{int}} = 14.25$ mm, height $h = 6$ mm. The thickness of mould walls is $t = 2$ mm. A sketch of the mould is shown in Fig. 2. Toroids are wound with different number of turns, for example $n_t = 30$ turns, of a round wire of diameter $\phi_s = 0.2$ mm. This diameter is convenient for reducing both temperature and proximity effects on the resistance of the wire, whereas it has not influence on the inductance. Pictures of wound samples corresponding to the toroid filled with dust and the concrete toroid are shown in Fig. 3.

Resistance and inductance of samples are measured by means of the Agilent E4980A LCR meter. This simple measurement option combined with an oven specifically designed for this characterization allows to obtain results at wide frequency range (from dc up to 2 MHz) and temperature range (from room temperature up to $250\,^{\circ}\text{C}$). Moreover, excitation current level can also be configured according to the characteristics of the LCR. The main advantage of this setup is that impedance is measured with high precision. However, power losses can not be measured with this arrangement due to the low excitation level and the low permeability of samples. In any case, power losses are provided by the manufacturer [47]. For the same reasons, saturation of the material at room temperature can not be achieved with this setup. Saturation measurements in specimens with low permeability require specific instrumentation with high rated current level and also require an specific design of samples in order to prevent the windings from overheating. Some characterization results are shown in Fig. 4. Resistance values (not represented here) reflect the increment of copper resistivity of the windings due to temperature increase and therefore they not have special interest. Moreover, inductance quickly falls down at temperatures above $200\,^{\circ}\text{C}$, which is similar to the Curie's temperature of some popular ferrites as the Ferroxcube 3C90 material [49]. Moreover, in Fig. 4 is also shown that the inductance is invariant with respect to frequency, at the considered range.

TABLE I: Composition by weight of MC40

Material	Phase	Element	% by weight
Magment MC40	magnetic	fine dust	43.5
		ferrite bits	43.5
	structural	cement	13.0

Magnetic permeability can be deduced from inductance measurements by means of simple integral operations involving Ampère's law and magnetic flux calculation in the toroid [50]

$$\mu_{\text{r}} = 1 + \frac{\frac{2\pi}{\mu_0 n_t^2} L - (h+2t)\ln\left(\frac{r_{\text{ext}}+t}{r_{\text{int}}-t}\right)}{h\ln\left(\frac{r_{\text{ext}}}{r_{\text{int}}}\right)}, \tag{1}$$

where L is the measured inductance. Fig. 4(a) shows the dependence with respect to the temperature of the relative permeability of samples at 100 kHz. Due to the low excitation level, the obtained permeability rather corresponds to the so called initial permeability. Results show that samples with ferrite bits have higher permeability than other samples. Considering this group, MC40 concrete has superior performance than cement, probably because the curing process reduces the air gap between ferrite bits. In any case, according to these results operation above $T = 150\,^{\circ}\text{C}$ should be carefully analyzed in order to avoid saturation effects. In addition Fig. 4(b) represents the inductance with respect to the frequency of the MC40 concrete for some selected temperatures. As it is represented, the value of the inductance is approximately constant at the considered frequency range.

III. Finite Element modeling and simulation

As it was above commented, the objective of this work is focused on evaluating alternatives to ferrite cores rather than design a specific application. Therefore, Finite Element electromagnetic simulations are obtained with the purpose of analyzing the effect of both the magnetic permeability and the thickness of a disk-shaped flux concentrator on the performance (mutual coupling and quality factor) of an IPT system. Fig. 5 shows the side view of a typical IPT system, which consists of two coils, namely transmitter TX and receiver RX coils hereinafter referred as 1 and 2 coils, respectively, flux concentrators and aluminum shielding. This figure represents misalignment between TX and RX coils. Coils are modeled by ring-shaped current densities flowing through ideal nondissipative media and, therefore, coils have no ohmic losses in this model. However, permeability of flux concentrators has some influence on the proximity losses of coils and for this reason actual losses are calculated afterwards following a specific loss model and calculation methodology [51]. Aluminum shielding is a dissipative medium and characterized by its electrical conductivity. The influence of shielding on the quality factor of the system is evident and, for this reason, shielding must be included in the model.

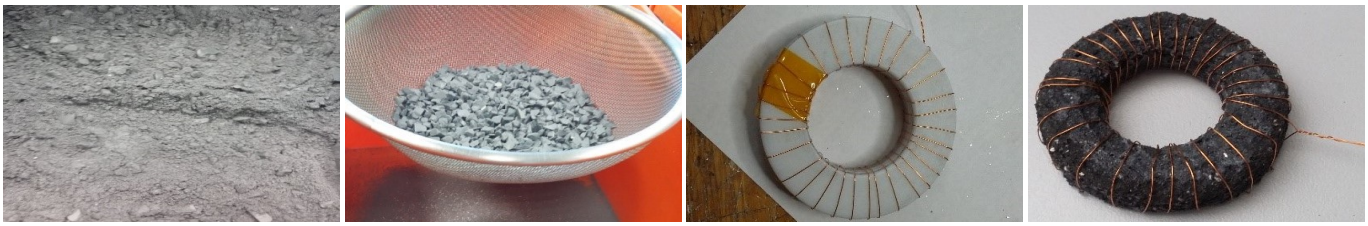

(a) (b) (c) (d)

Fig. 3: Images of the material characterization process. (a) MC40 cement. (b) Phases after sifting. (c) Sample for dust characterization. (d) Sample for concrete characterization.

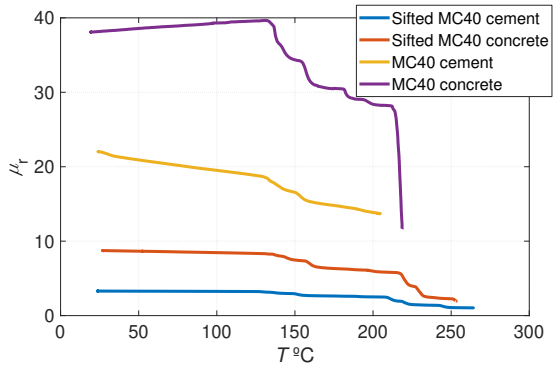

Fig. 4: Results of measurements of sample. (a) Relative permeability vs temperature for samples at 100 kHz. (b) Inductance vs frequency of the MC40 concrete for different temperatures.

According to the previous considerations, coils are defined by means of an impressed constant current density

$$\mathbf{J}_i = \frac{I_i}{S_{\text{turn\_}i}}\hat{\boldsymbol{\varphi}}_i = n_i\frac{I_i}{S_{\text{coil\_}i}}\hat{\boldsymbol{\varphi}}_i \qquad i = 1, 2, \tag{2}$$

where $\hat{\boldsymbol{\varphi}}_i$ is the direction of the current of the i^{th} coil in its local cylindrical coordinate system and n_i the number of turns. The current driven by the coil is $i_i = I_i e^{j\omega t}$, with ω being the angular frequency. Moreover, $S_{\text{turn\_}i}$, $S_{\text{coil\_}i}$ are the turn and the coil cross-sectional areas, respectively.

In systems with multiple coils, is convenient to use a matrix notation in order to represent the voltages and currents connection

$$\begin{bmatrix} V_1 \\ V_2 \end{bmatrix} = \begin{bmatrix} Z_{11} & Z_{12} \\ Z_{21} & Z_{22} \end{bmatrix} \cdot \begin{bmatrix} I_1 \\ I_2 \end{bmatrix}. \tag{3}$$

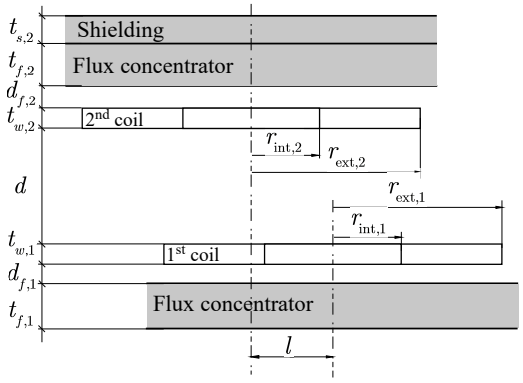

Fig. 5: 2D finite element model including the geometrical parameters.

Self impedance Z_{ii} relates the voltage drop across a coil to its current when the other coil is turned off. Similarly, mutual impedance Z_{ij} corresponds to the voltage of the i^{th} coil due to the current through the j^{th} coil. Therefore, in order to obtain any impedance is necessary to calculate the voltage of coils, which can be carried out by postprocessing the fields obtained in the simulations

$$V_i = -\int \mathbf{E}_i \cdot d\mathbf{l}_i = -\frac{n_i}{S_{\text{coil\_}i}}\int_{V_{\text{coil\_}i}} E_{\varphi\_i} dv \qquad i = 1, 2, \tag{4}$$

where E_{φ_i} is the electrical field in the i^{th} coil. Therefore

$$Z_{ij} = \left.\frac{V_i}{I_j}\right|_{I_{j'\neq j}=0} \qquad i, j = 1, 2. \tag{5}$$

The imaginary part of the cross terms of impedance corresponds to the mutual inductance between coils, M_{ij}.

Regarding winding losses, assuming that they are made of litz wire, they are calculated with the field results obtained for the nondissipative coil model and with the skin and proximity resistance formulas for litz wires. This calculation method is based on the following assumptions:

- Wires present perfect litz wire structure and therefore all strands are equivalent.
- The presence of wires do not modify the field obtained with the nondissipative coil simulations.
- Formulas strictly valid for the case of infinitely-long and isolated round strands are used to calculate the ac losses.

Considering that coils are wounded with litz wires of $n_{s,i}$ strands of radii $r_{s,i}$, the resistance including both dc and skin effect of the i^{th} coil is [52]

$$R_{\text{cond},i} = \frac{n_i}{n_{s,i}} \frac{\text{MLT}}{\sigma_w \left(\pi r_{s,i}^2\right)} \Phi_{\text{cond}} \left(\frac{r_{s,i}}{\delta}\right) \qquad i = 1, 2, \quad (6)$$

where σ_w is electrical conductivity of the wire, δ is the skin depth at a particular frequency, MLT_i is the mean length of turn of the i^{th} coil, and $\Phi_{\text{cond}}\left(r_{s,i}/\delta\right)$ is the ac resistance of a strand per unit of length. A usual design criterium is that the strand radius is of the same order or smaller than the skin depth at the working frequency. Under this condition, commonly referred as low-frequency regime [53], $R_{\text{cond},i}$ is reduced to the dc resistance of the coil.

Regarding the proximity losses of the coils, as it well known they have a purely ac nature, and they are generated because the conductors of the coils are immersed in an external varying magnetic field. The proximity losses of the conductors are proportional to the squared amplitude of the external magnetic field multiplied by the length of the conductor [54], $P_{\text{prox,conductor}} \propto \int_{l_{conductor}} \left|\overline{\mathbf{H}}\right|^2 dl$, where $l_{\text{conductor}}$ is the conductor length, $\overline{\mathbf{H}}$ is the normalized amplitude of the field per unit of Ampère. Moreover, as time-harmonic dependency is assumed, therefore $\left|\overline{\mathbf{H}}\right|^2$ corresponds to the modulus of the squared field amplitude.

Usually the squared amplitude of the magnetic field over the conductor is approximated by the mean value in the cable's cross-sectional area. In the case of analyzing a coil by means of a FEA tool, both this approximation and the previous expression for the length of the coil can be taken into account by means of the compact expression

$$\left\langle \left|\overline{\mathbf{H}}_i\right|^2 \right\rangle_{\text{coil},j} = \frac{n_{\text{coil},j}}{S_{\text{coil},j}} \int_{V_{\text{coil},j}} \left|\overline{\mathbf{H}}_i\right|^2 dv \qquad i, j = 1, 2, \quad (7)$$

where $S_{\text{coil},j}$ is the cross-sectional area, $V_{\text{coil},j}$ is the volume, and n_{coil_j} is the number of turns of the j^{th} coil, respectively.

Considering a system of several coils, it is worthwhile to mention that each coil induces proximity losses in its turns, denoted as $R_{\text{prox},i\to i}$, and in the turns of the other coil, $R_{\text{prox},i\to j}$. The first proximity losses contribution is [55]

$$R_{\text{prox},i\to i} = n_{s,i} n_i \frac{4\pi}{\sigma_w} \Phi_{\text{prox}} \left(\frac{r_{s,i}}{\delta}\right) \left\langle \left|\overline{\mathbf{H}}_i\right|^2 \right\rangle_{\text{coil},i} \quad i = 1, 2, \quad (8)$$

and the second is

$$R_{\text{prox},i\to j} = n_{s,j} n_j \frac{4\pi}{\sigma_w} \Phi_{\text{prox}} \left(\frac{r_{s,j}}{\delta}\right) \left\langle \left|\overline{\mathbf{H}}_i\right|^2 \right\rangle_{\text{coil},j} \qquad i, j = 1, 2 \quad i \neq j, \quad (9)$$

where $\left\langle \left|\overline{\mathbf{H}}_i\right|^2 \right\rangle_{\text{coil},i}$ and $\left\langle \left|\overline{\mathbf{H}}_i\right|^2 \right\rangle_{\text{coil},j}$ are the above defined field quantities per Ampère generated by the i^{th} coil in the volume occupied by the coils i^{th} and j^{th}, respectively. These values depend on the properties and position of flux concentrators and shielding, and therefore depends on the field solution for the complete model. These magnitudes give an intuitive idea of the proximity loss magnitude in a coil. $\Phi_{\text{prox}}\left(r_{s,i}/\delta\right)$ accounts for the ac dependency of the proximity losses of the strand. As in the previous case, for typical designs $r_{s,i}/\delta \leq 1$. In these conditions, usually the following approximation is adopted [56]:

$$\Phi_{\text{prox}} \left(\frac{r_{s,i}}{\delta}\right) \approx \frac{1}{4} \left(\frac{r_{s,i}}{\delta}\right)^4 \qquad i = 1, 2. \quad (10)$$

Apart from the winding losses, some power is also dissipated in the shielding. This power can be calculated by means of the Poynting's vector flux through the shielding surface, and can be represented as an equivalent resistance associated with each coil. Therefore, the resistance associated with the i^{th} coil is given by

$$R_{\text{sh},ii} = \text{Re}\left[\int_{S_{\text{sh}}} \left[\left(\overline{\mathbf{E}}_i \times \overline{\mathbf{H}}_i^{\,*}\right) \hat{\mathbf{n}}\right] dS_{\text{sh}}\right] \qquad i = 1, 2, \quad (11)$$

where $\hat{\mathbf{n}}$ is the normal vector to the shielding surface and bars over the fields represent per Ampère values. Considering (6), (8), (9) (11), the self resistance of the i^{th} coil is

$$R_{ii} = R_{\text{cond},ii} + R_{\text{prox},ii} + R_{\text{sh},ii} \qquad i = 1, 2 \quad i \neq j, \quad (12)$$

where $R_{\text{prox},ii} = R_{\text{prox},i\to i} + R_{\text{prox},i\to j}$. It also results of interest to express the factor kQ of an IPT system with respect to the above magnitudes for analyzing the impact of different parameters on efficiency. As it was pointed out by some authors, the kQ factor is a figure of merit of an IPT system whose maximization lead to maximum efficiency of energy transference [27]–[29], [57]. Therefore, considering

$$k = \frac{M_{12}}{\sqrt{L_{11} L_{22}}}, \quad , \quad (13)$$

and

$$Q = \sqrt{\frac{\omega_o L_{11}}{R_{11}} \cdot \frac{\omega_o L_{22}}{R_{22}}}, \quad (14)$$

where ω_o is the operating angular frequency, the factor kQ becomes

$$kQ = \frac{\omega_o M_{12}}{\sqrt{R_{11} R_{22}}}. \quad (15)$$

In order to analyze the influence of the thickness and permeability of the RX flux concentrator, FEA simulations of the system shown in Fig. 5 were carried out. For this purpose, a 2D model is analyzed where coils are aligned and, consequently, flux concentrators are modelled by means of disks. The internal and external radii of coils are $r_{\text{int}} = 100$ mm and $r_{\text{ext}} = 200$ mm, respectively. Vertical distance between coils is $d = 100$ mm. Flux concentrator disks are placed at $d_{f,i} = 1.5$ mm from coils, and diameters of disks and coils are identical. In this study, the permeability and the thickness of the disk beneath the TX coil are varied in order to analyze the effect of the material in the electrical parameters of the IPT system. The relative permeability is varied from $\mu_r = 1$ to $\mu_r = 1000$, thus this study covers materials with

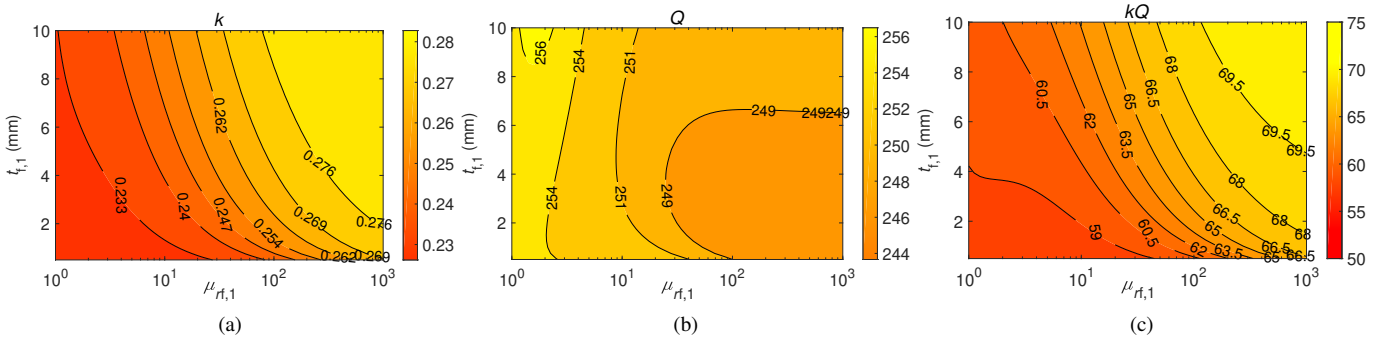

Fig. 6: Simulation results of the effect of relative permeability and thickness of the ferrite disk. (a) Coupling coefficient. (b) Quality factor of the IPT system. (c) kQ factor.

magnetic properties ranging from air to ferrite. The disk above the RX coil is a ferrite of $\mu_r = 1000$. An aluminium disk is also placed above the ferrite of the upper coil to partly shield the leakage fields.

Fig. 6 shows the simulated values of k, Q, and kQ. Regarding the coupling coefficient, simulations point that the dependencies of k with respect to relative permeability and thickness of the disk are similar. As it can be deduced from these results, it is possible to achieve the 93% of the maximum coupling by using a flux concentrator disk of thickness $t_{\mathrm{f},1} = 5$ mm and permeability of $\mu_{\mathrm{r},1} = 30$. Regarding the quality factor, it is observed that it mainly depends on the relative permeability of the disk. This factor is lower at the highest permeability values due to the increase of the proximity effect losses. Moreover, the kQ factor shows non-uniform dependence with respect to the studied variables; however, at the considered conditions its values are comprised between 60 and 75. The main conclusion of this analysis is that the thickness of the concrete magnetic disk should be $t_{\mathrm{f},1} \geq 5$ mm and the relative permeability $\mu_{\mathrm{r},1} \geq 30$.

Apart from the 2D simulations, which allow computational cost savings, a 3D FEA model was also developed in order to represent conventional systems including a ferrite sheet and an aluminum plate modelling the vehicle, as it is suggested in the J2954 standard. An exploded image of the developed 3D FEA model is shown in Fig. 7.

IV. Experimental verification

Considering the elements of the above mentioned IPT system, several prototypes corresponding to different configurations were tested. Fig. 8 shows different parts of the experimental setup. First, Fig. 8(a) shows the ferrite sheet. This sheet is made of conventional I-core ferrites of the TDK N87 material. The sheet is almost a square whose side is slightly larger than the diameter of the magnetizable concrete disk. Moreover, the thickness of the ferrite sheet matches the thickness of the concrete disk. Fig. 8(b) shows the magnetizable concrete disk. Fig. 8(c) shows the practical implementation of coils, and finally the IPT system is shown in Fig. 8(d). The main parameters of the system are listed in Table II. Among other parameters, it is shown that the weight of concrete disk is about the 62% of the weight of the ferrite sheet.

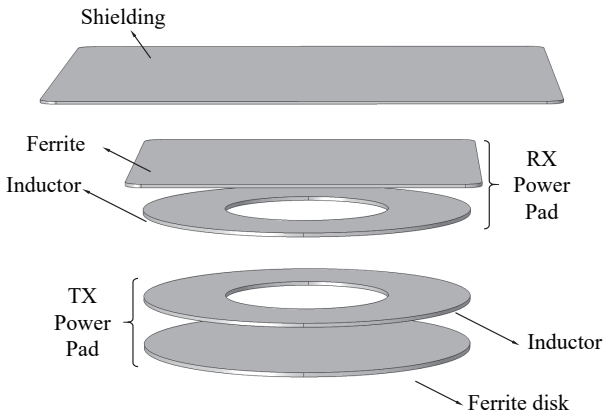

Fig. 7: 3D finite element model for simulating an IPT system with a magnetizable concrete disk and a ferrite sheet and aluminum shielding.

These elements allows to test up to three different configurations of the TX power pad. These configurations are:

- Coil in air.
- Coil with a ferrite sheet.
- Coil with a magnetizable concrete disk.

The first configuration is convenient to check the accuracy of the loss modeling of cables, which in its turn affects to the quality factor of coils. The second configuration corresponds to the conventional arrangement of IPT systems. The third configuration is the new proposal of this work. On the other hand, the considered configuration for the RX pad includes a ferrite sheet of the same dimensions of the TX, and an 80×80 aluminum sheet, which emulates the vehicle.

Impedance measurements were also carried out by means of the Agilent E4980A LCR meter. Non-diagonal matrix impedance terms can be experimentally obtained by using two measurements according to two different connections of coils, namely in-phase, $Z_{\mathrm{i\_p}}$, and anti-phase, $Z_{\mathrm{a\_p}}$, connections. According to these connections, the measured impedances corresponds to $Z_{i\_p} = Z_{11}+Z_{22}+2Z_{12}$, $Z_{a\_p} = Z_{11}+Z_{22}-2Z_{12}$. Therefore

$$Z_{12} = Z_{21} = \frac{Z_{\mathrm{i\_p}} - Z_{\mathrm{a\_p}}}{4} \tag{16}$$

First tests were carried out with the TX single coil in the

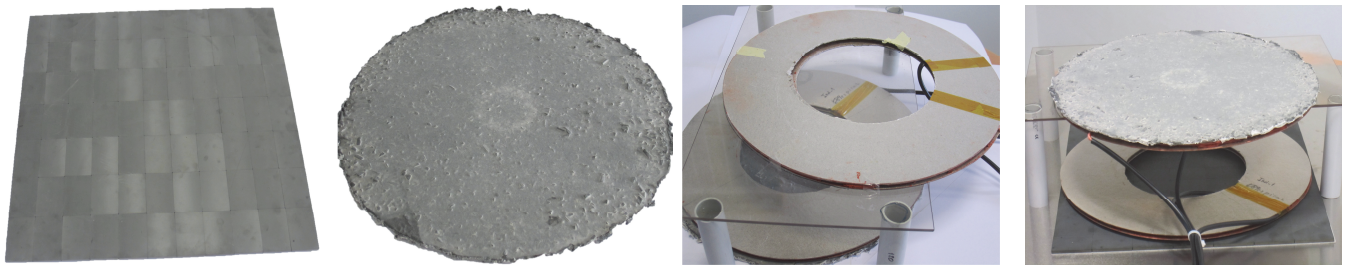

(a) (b) (c) (d)

Fig. 8: Images of the experimental setup. (a) Ferrite sheet. (b) Magnetizable concrete disk. (c) Coils. (d) System with aluminum plate.

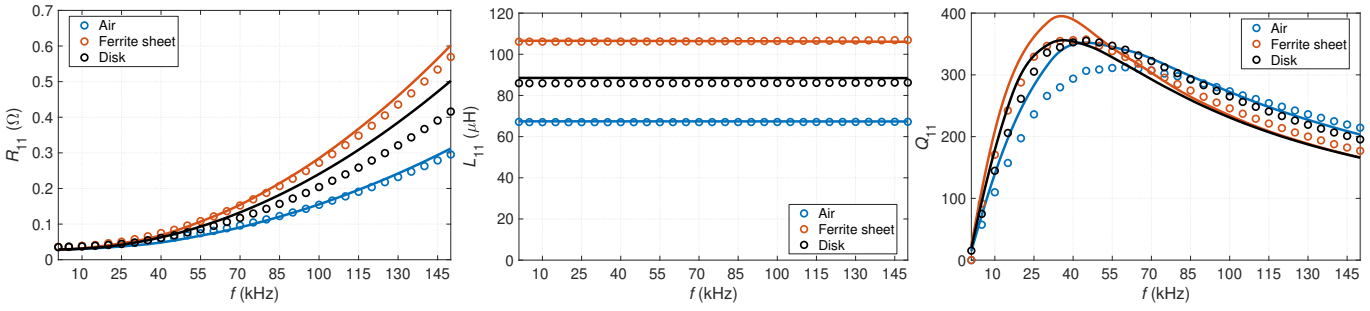

(a) (b) (c)

Fig. 9: Simulated and measured results for a single power pad in three configurations: air, ferrite sheet and magnetizable concrete disk. (a) Resistance. (b) Inductance. (c) Quality factor.

TABLE II: Parameters of the elements of the experimental setup.

Description	Symbol	Value	Units
Number of turns	n_1, n_2	9	[-]
Internal radius	$r_{\text{int},1}, r_{\text{int},2}$	100	[mm]
External radius	$r_{\text{ext},1}, r_{\text{ext},2}$	200	[mm]
Winding thickness	$t_{w,1}, t_{w,2}$	4.5	[mm]
Distance ferrite-winding	$d_{f,1}, d_{f,2}$	1.5	[mm]
Concrete magnetic disk radius	$r_{f,1}$	102.5	[mm]
Concrete disk thickness	$t_{f,1}$	5	[mm]
Concrete disk weight	$W_{f,1}$	2.5	[kg]
Concrete relative permeability (room T)	$\mu_{rf,1}$	38	[-]
Thickness of ferrite sheet	$t_{f,2}$ or $t_{f,1}$	5	[mm]
Dimensions of ferrite sheet	-	409×419	[mm]
Relative permeability of ferrite sheet	$\mu_{rf,2}$	1000	[-]
Shielding thickness	$t_{s,2}$	3	[mm]
Shielding dimensions	-	80×80	[mm]
Ferrite sheet weight	$W_{f,2}$	4	[kg]
Aluminium conductivity	σ_{Al}	$2 \cdot 10^7$	[S/m]
Cable type		Litz wire	
Number of strands	$n_{s,1}, n_{s,2}$	200	[-]
Strand diameter	$\phi_{s,1}, \phi_{s,2}$	200	[μm]
Distance range	$100 \leq d \leq 200$		[mm]
Misalignment range	$0 \leq l \leq 200$		[mm]

three mentioned configurations. In this case the resistance and inductance of a coil were simulated and measured with respect to frequency for a set of frequencies ranging from 1 kHz to 150 kHz. Moreover, the Q factor of the coil was also calculated with the resistance and inductance values. The measured and simulated results are shown in Fig. 9.

As it is shown, the quality factor with the ferrite sheet is higher than in the other configurations. However, as it can be observed, the quality factor with the concrete disk is of the same order. It is clear that the self inductance increases with the ferrite sheet but the proximity losses are also penalized. Both effects are similar and therefore they compensate each other. Simulated and measured results show good agreement and this fact points that the developed model is appropriate.

The second set of experiments was accomplished with the two coils concentrically placed and varying the distance between them. Accordingly, these tests corresponds to the case $100 \leq d \leq 150$ mm and $l = 0$. In this case the considered configurations for the TX power pad were air, ferrite sheet and magnetizable concrete disk, whereas the configuration of the RX power pad was the same for the three mentioned cases and consisted of the coil with the ferrite sheet and the aluminum shielding. Measurements were carried out at 85 kHz. Simulated and measured results are shown in Fig. 10. As expected, the coupling factor decreases for increasing distances between coils. However, the quality factor is nearly invariant with respect to this distance. According to (14), both self-inductance and self-resistance of each power pad are mainly dependent of its sizing and its closest materials, whereas the size and materials of the other distantly-located elements have a minor influence. As in the previous case, power pads with ferrite sheet present the best results, in terms of the kQ parameter. However, the results achieved with the magnetizable concrete are of the same order and the differences are smaller when the distance is increased. The highest observed difference is about the 10%, corresponding to kQ values of 80 and 71, 6, respectively for 100 mm of

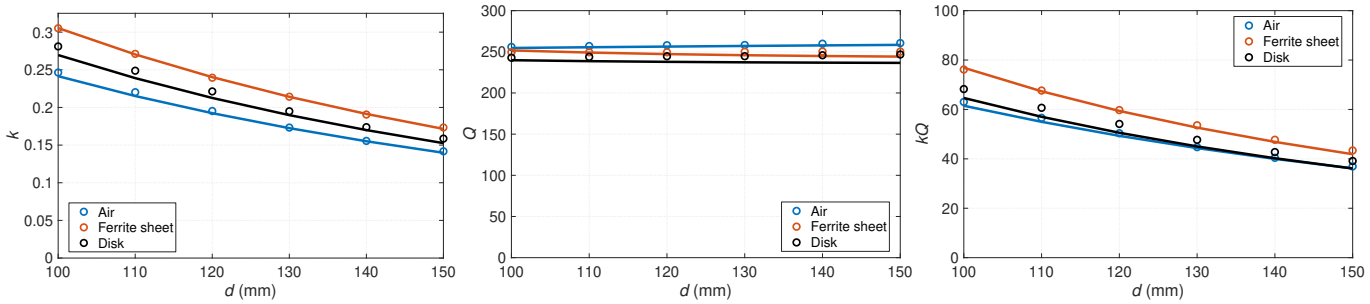

Fig. 10: Simulated and measured results for the concentrically placed power pads with three configurations of the TX pad: air, ferrite sheet and magnetizable concrete disk. (a) k. (b) Q. (c) kQ.

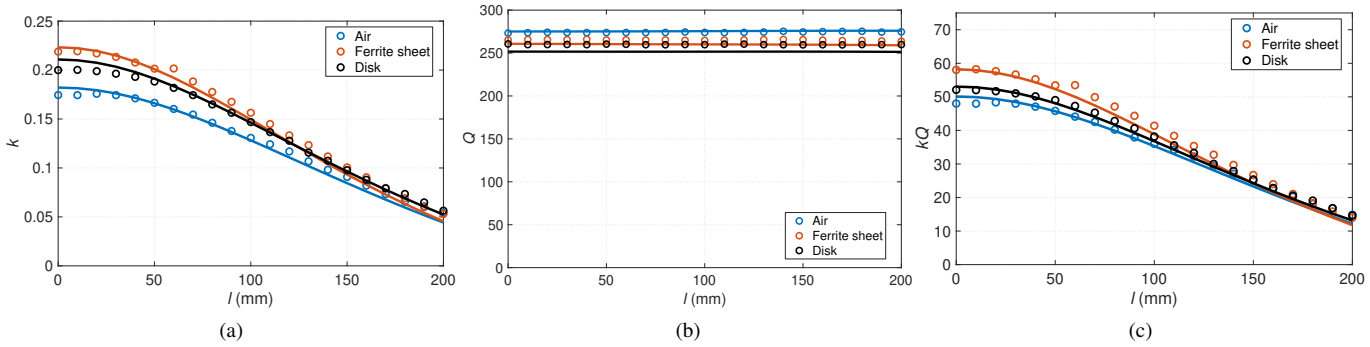

Fig. 11: Simulated and measured results of the IPT system with respect to the misalignment between coils in three configurations of the TX pad: air, ferrite sheet and magnetizable concrete disk. (a) k. (b) Q. (c) kQ.

distance, whereas the difference is the 6.6% (42 and 45) for 150 mm of distance. It is also interesting to note that the observed reduction of kQ due to the distance is about the 50%.

A third set of measurements was also completed, in this case with the purpose of analyzing the effect of the misalignment between the power pads. The results are shown in Fig. 11. As in the previous case, impedance values were measured at 85 kHz and the conditions of measurements were $d = 120$ mm and $0 \leq l \leq 200$ mm. As it can be observed, the tendencies of parameters k and Q with respect to misalignment are similar to those observed in the previous cases. The difference between the ferrite sheet and the concrete disk for the aligned case is about 12%, whereas this difference is less than 5% for a misalignment of 200 mm.

The magnetizable concrete was tested in a real experiment with a transmitted power higher than 5 kW. The primary of the IPT system was fed by means of a full bridge series-compensated resonant inverter featuring a 1200 V, 50 A cool SiC INFINEON FF23MR12W1M1B11 BOMA1 module. The compensation of the secondary was also a series capacitor. The secondary voltage was rectified by means of a full bridge of 1.2 kV, 60 A ST STTH12012TV1 ultrafast diodes and the dc output was filtered by means of a LC network. The output was connected to a programmable electronic load. The LC filter was required in order to prevent from high ripple in the electronic load. In this case the LC filter was not optimized because it is not an objective of this work. For this

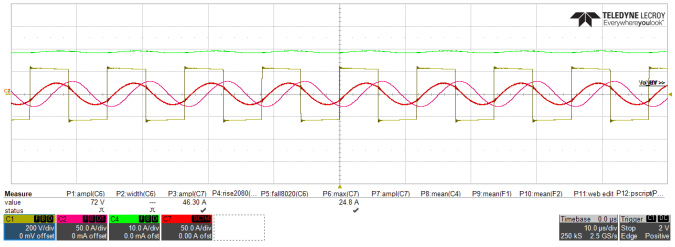

Fig. 12: Experimental results. Waveforms for the case of 5 kW of transmitted power.

reason, high losses in the filter's inductance were observed and, consequently, the global efficiency of the IPT system was about the 80%. The operating frequency was set at $f = 85$ kHz and the compensation capacitor values were $C_{r1} = 40.5$ nF and $C_{r2} = 33.5$ nF.

Fig. 12 shows some waveforms corresponding to a transmitted power of 5 kW. In this figure C1 corresponds to the primary full-bridge inverter output voltage, C2 is the primary current, C4 is the current of the electronic load, and C7 the current of the secondary. As it is shown, the primary and secondary currents are well balanced, which is due to the used series-series compensation. The electronic load voltage was about 260 V and the current was 19 A. On the other hand, primary and secondary currents were about 20 A rms.

The temperature reached by the primary and secondary coils was about 33 °C after half an hour of working, for 21 °C of room temperature. The magnetic concrete temperature was

TABLE III: Performance matrix comparison.

Parameter	Magnetizable concrete	Ferrite
Cost	Some extra cost with respect to the regular concrete	The cost of the ferrite should be added to the cost of the concrete
Mechanical strength	Determined by the strength of the structural phase of the cement	Ceramic brittle material
Compatibility with the roadway	Magnetizable concrete adapts the roadway characteristics, as the shape	The roadway shape should be conformed by means of available ferrite cores.

lower, about $30\,^{\circ}\mathrm{C}$.

V. Discussion

According to the precedent results, the electrical parameters k, Q and kQ of the magnetizable concrete are in between the air and the ferrite. Apart from these parameters, other aspects are qualitatively compared in Table III.

The main advantages of the magnetizable concrete derives from the fact that some magnetic permeability is incorporated to the concrete and, therefore, the addition of an extra element to the application is avoided. The cost of the magnetic concrete is higher than the cost of regular concrete because it should include the cost of the ferrite bits and dust (which depend on materials and quantities) but the cost of the ferrite and its corresponding installation are avoided. The mechanical strength of the magnetizable concrete depends on the mechanical properties of the structural phase of the cement. However, ferrite is a ceramic brittle material. Moreover, ferrites should be firmly mounted in order to avoid displacements which could lead to road deformations. Regarding the compatibility with the roadway, to construct a roadway fully incorporating ferrites could be unpractical and expensive whereas the magnetizable concrete naturally provide some magnetic permeability to the full roadway.

The possibility of achieving a magnetizable concrete arrangement with the same performance of the ferrite sheet has also been analyzed. For this purpose, a study of the performance with respect to the thickness of the concrete disk was carried out by means of 3D FEA simulations, where the thickness was varied from 5 mm to 100 mm. In this study, the concrete permeability was $\mu_{rf,1} = 38$, coils were aligned and the distance between them was $d = 100$ mm. These results are compared with the case of a ferrite sheet of thickness $t_{f,1} = 5$ mm, $\mu_{rf,1} = 1000$ and results are presented in Fig. 13. As it can be observed, the performance of the concrete is asymptotic with respect to its thickness. In view of these results, both fully-covered-ferrite and fully-ferrite-equivalent-concrete options could be unpractical. Therefore, an intermediate balanced arrangement could be an interesting option.

Additionally, a concrete disk with double thickness was also built and tested. Experimental results with respect to misalignment (for a distance of $d = 110$ mm) are presented in Fig. 14, where the four configurations of the TX power pad are compared: air, ferrite sheet, magnetizable concrete disk and double-thickness magnetizable concrete disk. In this figure is evident the effect of the magnetizable concrete disk thickness because the double-thickness disk is in between of the single-thickness and ferrite sheet performances.

VI. Conclusion

In this work, the characteristics of a magnetizable concrete are studied having in mind a potential application in IPT systems. The tested magnetic cement contains ferrite dust and bits conferring a relative permeability in the range of tens to the resultant concrete. The different phases of the material (sifted cement, cement and concrete) are tested and it is concluded that the final properties are mainly determined by the ferrite type and composition by weight. Measurements of Curie's temperature and permeability at different frequencies are also presented. A 2D finite element simulation model is developed and used for predicting the convenient values of permeability and thickness of the magnetizable concrete disk. Simulations point out that when relative permeability is about several tens and the minimum thickness is 5 mm and, the 93% of maximum coupling is achieved. A 3D finite element simulation model is also developed with the purpose of verifying the experimental results. To this end, a versatile IPT experimental system was planned with different arrangements. From the obtained results, it is concluded that magnetizable concrete with $t = 5$ mm of thickness and $\mu_r = 38$ of relative permeability presents a kQ value about 90% of the kQ value with a ferrite sheet for the aligned case and 100 mm of distance. The difference of the kQ values is smaller when both the distance of misalignment are increased. In this case, the kQ with the magnetizable concrete could reach 95% of the value achieved with the ferrite sheet. An analysis of the concrete thickness required to achieve equivalent performance of the ferrite sheet has been also conducted. Simulation and experimental results show that the higher the thickness is, the better performance is achieved. However, an asymptotic tendency is observed, pointing that high increments of thickness result in small performance improvements.

Acknowledgment

This work was supported in part by the Spanish MINECO under Project TEC2016-78358-R, Project RTC-2017-5965-6, by the Gobierno de Aragón-FSE 2014-20, and by the BSH Home Appliances Group.

References

[1] G. Covic and J. Boys, "Modern trends in inductive power transfer for transportation applications," *IEEE Trans. Emerg. Sel. Topics Power Electron.*, vol. 1, pp. 28–41, Mar. 2013.

[2] ——, "Inductive power transfer," *Proc. IEEE*, vol. 101, pp. 1276–1289, Jun. 2013.

[3] Z. Zhang, H. Pang, A. Georgiadis, and C. Cecati, "Wireless power transfer-an overview," *IEEE Trans. Ind. Electron.*, vol. 66, pp. 1044–1058, Feb. 2019.

[4] D. H. Tran, V. B. Vu, and W. Choi, "Design of a high-efficiency wireless power transfer system with intermediate coils for the on-board chargers of electric vehicles," *IEEE Trans. Power Electron.*, vol. 33, pp. 175–187, Jan. 2018.

[5] E. Gati, G. Kampitsis, and S. Manias, "Variable frequency controller for inductive power transfer in dynamic conditions," *IEEE Trans. Power Electron.*, vol. 32, pp. 1684–1696, Feb. 2017.

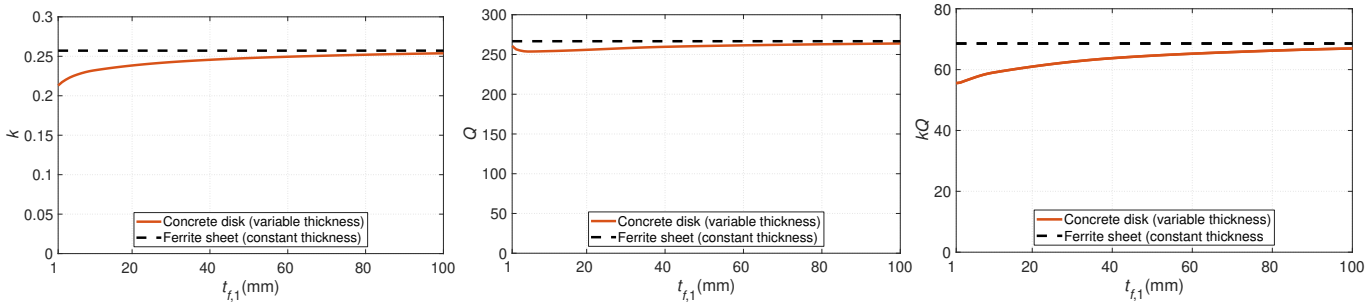

Fig. 13: Comparison of the performance of a magnetizable concrete disk with variable thickness with respect to the ferrite sheet. (a) k. (b) Q. (c) kQ.

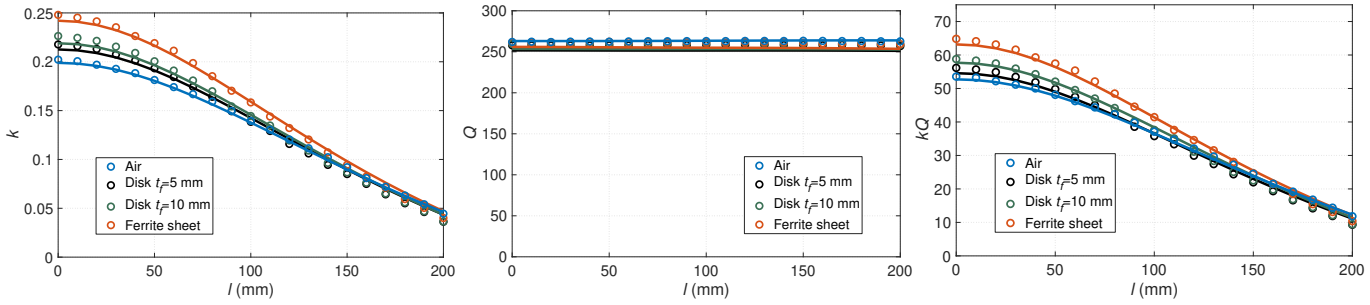

Fig. 14: Simulated and measured results of the IPT system with respect to the misalignment between coils in four configurations of the TX pad: air, ferrite sheet, magnetizable concrete disk and double-thickness magnetizable concrete disk. (a) k. (b) Q. (c) kQ.

[6] Q. Li and Y. Liang, "An inductive power transfer system with a high-Q resonant tank for mobile device charging," *IEEE Trans. Power Electron.*, vol. 30, pp. 6203–6212, Nov. 2015.

[7] S. Li and C. C. Mi, "Wireless power transfer for electric vehicle applications," *IEEE Trans. Emerg. Sel. Topics Power Electron.*, vol. 3, pp. 4–17, Jan. 2015.

[8] S. Tang, T. L. Lun, Z. Guo, K. Kwok, and N. McDannold, "Intermediate range wireless power transfer with segmented coil transmitters for implantable heart pumps," *IEEE Trans. Power Electron.*, vol. 32, pp. 3844–3857, May 2017.

[9] W. Wang, X. Huang, J. Guo, H. Liu, C. Yan, and L. Tan, "Power stabilization based on efficiency optimization for WPT systems with single relay by frequency configuration and distribution design of receivers," *IEEE Trans. Power Electron.*, vol. 32, pp. 7011–7024, Sep. 2017.

[10] C. Mi, G. Buja, S. Choi, and C. Rim, "Modern advances in wireless power transfer systems for roadway powered electric vehicles," *IEEE Trans. Ind. Electron.*, vol. 63, pp. 6533–6545, Oct. 2016.

[11] A. Kamineni, M. J. Neath, G. A. Covic, and J. T. Boys, "A mistuning-tolerant and controllable power supply for roadway wireless power systems," *IEEE Trans. Power Electron.*, vol. 32, pp. 6689–6699, Sep. 2017.

[12] T. Kan, R. Mai, P. Mercier, and C. Mi, "Design and analysis of a three-phase wireless charging system for lightweight autonomous underwater vehicles," *IEEE Trans. Power Electron.*, vol. 33, pp. 6622–6632, Aug. 2018.

[13] S. Du, E. Chan, B. Wen, J. Hong, H. Widmer, and C. Wheatley, "Wireless power transfer using oscillating magnets," *IEEE Trans. Ind. Electron.*, vol. 65, pp. 6259–6269, Aug. 2018.

[14] S. Lee and I. G. Jang, "Layout optimization of the receiver coils for multitransmitter wireless power transfer systems," *IEEE Trans. Emerg. Sel. Topics Power Electron.*, vol. 5, pp. 1311–1321, Sep. 2017.

[15] K. Lee and S. Chae, "Power transfer efficiency analysis of intermediate-resonator for wireless power transfer," *IEEE Trans. Power Electron.*, vol. 33, pp. 2484–2493, Mar. 2018.

[16] Q. Zhu, M. Su, Y. Sun, W. Tang, and A. Hu, "Field orientation based on current amplitude and phase angle control for wireless power transfer," *IEEE Trans. Ind. Electron.*, vol. 65, pp. 4758–4770, Jun. 2018.

[17] G. Zhu and R. D. Lorenz, "Achieving low magnetic flux density and low electric field intensity for a loosely coupled inductive wireless power transfer system," *IEEE Trans. Ind. Appl.*, vol. 54, pp. 6383–6393, Nov. 2018.

[18] W. Zhong and S. Hui, "Reconfigurable wireless power transfer systems with high energy efficiency over wide load range," *IEEE Trans. Power Electron.*, vol. 33, pp. 6379–6390, Jul. 2018.

[19] Y. Sun, Z. Liao, Z. Ye, C. Tang, and P. Wang, "Determining the maximum power transfer points for mc-wpt systems with arbitrary number of coils," *IEEE Trans. Power Electron.*, vol. 33, pp. 9734–9743, Nov. 2018.

[20] B. Choi, V. Thai, E. Lee, J. Kim, and C. Rim, "Dipole-coil-based wide-range inductive power transfer systems for wireless sensors," *IEEE Trans. Ind. Electron.*, vol. 63, pp. 3158–3167, May 2016.

[21] B. Choi, E. Lee, Y. Sohn, G. Jang, and C. Rim, "Six degrees of freedom mobile inductive power transfer by crossed dipole tx and rx coils," *IEEE Trans. Power Electron.*, vol. 31, pp. 3252–3272, Apr. 2016.

[22] E. Lee, , B. Choi, J. Choi, D. Nguyen, and C. Rim, "Wide-range adaptive ipt using dipole-coils with a reflector by variable switched capacitance," *IEEE Trans. Power Electron.*, vol. 32, pp. 8054–8070, Oct. 2017.

[23] R. Tavakoli and Z. Pantic, "Analysis, design, and demonstration of a 25-kw dynamic wireless charging system for roadway electric vehicles," *IEEE Trans. Emerg. Sel. Topics Power Electron.*, vol. 6, pp. 1378–1393, Sep. 2018.

[24] M. Lu and K. Ngo, "A fast method to optimize efficiency and stray magnetic field for inductive-power-transfer coils using lumped-loops model," *IEEE Trans. Power Electron.*, vol. 33, pp. 3065–3075, 4 2018.

[25] ——, "Systematic design of coils in series-series inductive power transfer for power transferability and efficiency," *IEEE Trans. Power Electron.*, vol. 33, pp. 3333–3345, Apr. 2018.

[26] C. Carretero, "Coupling power losses in inductive power transfer systems with litz-wire coils," *IEEE Trans. Ind. Electron.*, vol. 64, pp. 4474–4482, Jun. 2017.

[27] R. Bosshard, J. W. Kolar, J. Muhlethaler, I. Stevanovic, B. Wunsch, and F. Canales, "Modeling and η-α-Pareto optimization of inductive power transfer coils for electric vehicles," *IEEE Trans. Emerg. Sel. Topics Power Electron.*, vol. 3, pp. 50–64, Mar. 2015.

[28] R. Bosshard and J. W. Kolar, "Multi-objective optimization of 50 kW/85 kHz IPT system for public transport," *IEEE Trans. Emerg. Sel. Topics Power Electron.*, vol. 4, pp. 1370–1382, Dec. 2016.

[29] R. Bosshard, U. Iruretagoyena, and J. Kolar, "Comprehensive evaluation of rectangular and double-D coil geometry for 50 kW/85 kHz IPT system," *IEEE Trans. Emerg. Sel. Topics Power Electron.*, vol. 4, pp. 1406–1415, Dec. 2016.

[30] Y. Li, R. Mai, L. Lu, T. Lin, Y. Liu, and Z. He, "Analysis and transmitter currents decomposition based control for multiple overlapped transmitters based WPT systems considering cross couplings," *IEEE Trans. Power Electron.*, vol. 33, pp. 1829–1842, Jan. 2018.

[31] J. Zhang, X. Yuan, C. Wang, and Y. He, "Comparative analysis of two-coil and three-coil structures for wireless power transfer," *IEEE Trans. Power Electron.*, vol. 32, pp. 341–352, Jan. 2017.

[32] F. Liu, Y. Yang, D. Jiang, X. Ruan, and X. Chen, "Modeling and optimization of magnetically coupled resonant wireless power transfer system with varying spatial scales," *IEEE Trans. Power Electron.*, vol. 32, pp. 3240–3250, Apr. 2017.

[33] S. Kim, G. A. Covic, and J. T. Boys, "Tripolar pad for inductive power transfer systems for EV charging," *IEEE Trans. Power Electron.*, vol. 32, pp. 5045–5057, Jul. 2017.

[34] J. Zhao, T. Cai, S. Duan, H. Feng, C. Chen, and X. Zhang, "A general design method of primary compensation network for dynamic WPT system maintaining stable transmission power," *IEEE Trans. Power Electron.*, vol. 31, pp. 8343–8358, Dec. 2016.

[35] K. Chen and Z. Zhao, "Analysis of the double-layer printed spiral coil for wireless power transfer," *IEEE Trans. Emerg. Sel. Topics Power Electron.*, vol. 1, pp. 114–121, Jun. 2013.

[36] M. Liu, Y. Qiao, S. Liu, and C. Ma, "Analysis and design of a robust class E^2 dc-dc converter for megahertz wireless power transfer," *IEEE Trans. Power Electron.*, vol. 32, pp. 2835–2845, Apr. 2017.

[37] S. Cove, M. Ordonez, N. Shafiei, and J. Zhu, "Improving wireless power transfer efficiency using hollow windings with track-width-ratio," *IEEE Trans. Power Electron.*, vol. 31, pp. 6524–6533, Sep. 2016.

[38] I. Ortego-Isasa, K. Benli, F. Casado, J. Sancho, and D. Valderas, "Topology analysis of wireless power transfer systems manufactured via inkjet printing technology," *IEEE Trans. Ind. Electron.*, vol. 64, pp. 7749–7757, Oct. 2017.

[39] J. Acero, J. Serrano, C. Carretero, I. Lope, and J. Burdío, "Analysis and design of tubular coils for wireless inductive power transfer systems," in *Proc. 2017 IEEE APEC Conf.*, Mar. 2017, pp. 848–854.

[40] W. Roshen and D. Turcotte, "Planar inductors on magnetic substrates," *IEEE Trans. Magn.*, vol. 24, pp. 3213–3216, Nov. 1988.

[41] W. Roshen, "Analisys of planar sandwich inductors by current images," *IEEE Trans. Magn.*, vol. 26, pp. 2880–2887, Sep. 1990.

[42] C. Park, S. Lee, G. Cho, and C. Rim, "Innovative 5-m-off-distance inductive power transfer systems with optimally shaped dipole coils," *IEEE Trans. Power Electron.*, vol. 30, pp. 817–827, Feb. 2015.

[43] J. Kim, B. Lee, J. Lee, S. Lee, C. Park, S. Jung, K. Yi, and J. Baek, "Development of 1-MW inductive power transfer system for a high-speed train," *IEEE Trans. Ind. Electron.*, vol. 62, pp. 6242–6250, Oct. 2015.

[44] S. Choi, S. Jeong, B. Gu, G. Lim, and C. Rim, "Ultraslim S-type power supply rails for roadway-powered electric vehicles generalized models on self-decoupled dual pick-up coils for a large lateral tolerance," *IEEE Trans. Power Electron.*, vol. 30, pp. 6456–6468, Nov. 2015.

[45] G. Elliott, G. Covic, D. Kacprzak, and J. Boys, "A new concept: asymmetrical pick-ups for inductively coupled power transfer monorail systems," *IEEE Trans. Magn.*, vol. 42, pp. 3389–3391, Oct. 2006.

[46] M. Kissin, J. Boys, and G. Covic, "Interphase mutual inductance in polyphase inductive power transfer systems," *IEEE Trans. Ind. Electron.*, vol. 56, pp. 2393–2400, Jul. 2009.

[47] MAGMENT UG. [Online]. Available: http://magment.de/

[48] R. Tavakoli, A. Echols, U. Pratik, Z. Pantic, F. Pozo, A. Malakooti, and M. Maguire, "Magnetizable concrete composite materials for road-embedded wireless power transfer pads," in *Proc. 2017 IEEE Energy Conversion Congress and Exposition (ECCE)*, Oct. 2017, pp. 4041–4048.

[49] Ferroxcube, "Soft ferrites and accesories. data handbook," Tech. Rep., 2009 (accessed February, 2018). [Online]. Available: https://www.ferroxcube.com/en-global/download/download/11

[50] C. T. A. Johnk, *Engineering electromagnetics fields and waves*, 2nd ed., J. Sons, Ed., 2008.

[51] I. Lope, J. Acero, and C. Carretero, "Analysis and optimization of the efficiency of induction heating applications with litz-wire planar and solenoidal coils," *IEEE Trans. Power Electron.*, vol. 31, pp. 5089–5101, Jul. 2016.

[52] J. Lammeraner and M. Stafl, *Eddy Currents*, O. Chemical Rubber Co., Cleveland, Ed., 1964.

[53] R. Wojda and M. Kazimierczuk, "Analytical optimization of solid-round-wire windings," *IEEE Trans. Ind. Electron.*, vol. 60, pp. 1033–1041, 3 2013.

[54] J. Ferreira, "Appropriate modelling of conductive losses in the design of magnetic components," in *Proc. 21st Annual IEEE Conference on Power Electronics Specialists (PESC'90)*, Jun. 1990, pp. 780–785.

[55] C. Feeney, J. Zhang, and M. Duffy, "Ac winding loss of phase-shifted coupled windings," *IEEE Trans. Power Electron.*, vol. 31, pp. 1472–1478, Feb. 2016.

[56] C. Carretero, J. Acero, and R. Alonso, "TM-TE decomposition of power losses in multi-stranded litz-wires used in electronic devices," *Progress In Electromagnetics Research, PIER*, vol. 123, pp. 83–103, Jan. 2012.

[57] G. Vandevoorde and R. Puers, "Wireless energy tranfer for stand-alone systems: A comparison between low and high power applicability," *Sensors and Actuators A: Physical*, vol. 92, pp. 305–311, Jul. 2001.